Computers in Biology and Medicine 111 (2019) 103352

Contents lists available at ScienceDirect

Computers in Biology and Medicine

journal homepage: www.elsevier.com/locate/compbiomed

Multi-proportion channel ensemble model for retinal vessel segmentation

Peng Tang[a,b], Qiaokang Liang[a,b,*], Xintong Yan[a,b], Dan Zhang[c], Gianmarc Coppola[d], Wei Sun[a,b]

[a] College of Electrical and Information Engineering, Hunan University, Changsha, 410082, China
[b] National Engineering Laboratory for Robot Vision Perception and Control Technologies, Hunan Key Laboratory of Intelligent Robot Technology in Electronic Manufacturing, Changsha, 410082, China
[c] Department of Mechanical Engineering, York University, Toronto, ON, M3J 1P3, Canada
[d] Faculty of Engineering and Applied Science, University of Ontario Institute of Technology, Oshawa, Ontario, L1H 7K4, Canada

ARTICLE INFO

Keywords:
Computer-aided diagnosis
Deep learning
Retinal vessel segmentation
Multi-proportion channel ensemble model
Retinal fundus images

ABSTRACT

Objective: A novel supervised method that is based on the Multi-Proportion Channel Ensemble Model (MPC-EM) is proposed to obtain more vessel details with reduced computational complexity.

Methods: Existing Retinal Vessel Segmentation (RVS) algorithms only work using the single G channel (Green Channel) of fundus images because that channel normally contains the most details with the least noise, while the red and blue channels are usually saturated and noisy. However, we find that the images that are composed of the αG-channel and (1-α) R-channel (Red Channel) with different values of α produce multiple particular global features. This enables the model to detect more local vessel details in fundus images. Therefore, we provide a detailed description and evaluation of the segmentation approach based on the MPC-EM for the RVS. The segmentation approach consists of five identical submodels. Each submodel can capture various vessel details by being trained using different composition images. These probabilistic maps that are produced by five submodels are averaged to achieve the final refined segmentation results.

Results: The proposed approach is evaluated using 4 well-established datasets, i.e., DRIVE, STARE, HRF and CHASE_DB1, with accuracies of 95.74%, 96.95%, 96.31%, and 96.54%, respectively. Additionally, quantitative comparisons with other existing methods and cross-training results are included.

Conclusion: The segmentation results showed that the proposed algorithm based on the MPC-EM with simple submodels can achieve state-of-the-art accuracy with reduced computational complexity.

Significance: Compared with other existing methods that are trained using only the G channel and raw images, the proposed approach based on the MPC-EM, submodels of which are trained using different proportional compositions of R and G channels, obtains better segmentation accuracy and robustness. Additionally, the experimental results show that the R channel of fundus images can also produce performance gains for RVS.

1. Introduction

The analysis of blood vessels that are extracted from retinal fundus images is conventionally used by medical specialists to diagnose complicated diseases, including arteriosclerosis, diabetic retinopathy (DR), strokes and glaucoma [1]. Globally, the most common preventable blindness factors are age-related macular degeneration, glaucoma, and DR. The American Diabetes Association (ADA) reports that approximately 4.2 million adults have DR and 655 000 adults have vision-threatening DR or diabetes-related blindness. The corresponding treatments reached an annual high of US $500 million in the United States. The vision problems and blindness that are caused by DR may be prevented through the early detection and treatment of eye diseases [3]. Hence, the segmentation of retinal blood vessels on the fundus images, which is the key step of the early diagnosis, is important for the diagnosis and prevention of eye diseases.

Manual labelling of blood vessels in fundus images is a laborious and time-consuming task that is requiring professional experience and skills [4,5]. The extreme variations in the sizes, shapes and intensities of retinal vessel images in the different local region make it hard to obtain accurate segmentation results. In the development of Computer-aided diagnosis systems, automatic Retinal Vessel Segmentation (RVS is considered as the most critical step. Although numerous attempts have been made to address the challenge of the automatic RVS, this task is still an active area of research due to the benefits of having more accurate and robust results [6].

---

[*] Corresponding author. College of Electrical and Information Engineering, Hunan University, Changsha, 410082, China.

E-mail addresses: tangpeng@hnu.edu.cn (P. Tang), qiaokang@hnu.edu.cn (Q. Liang), yxt@hnu.edu.cn (X. Yan), dzhang99@yorku.ca (D. Zhang), Gianmarc.Coppola@uoit.ca (G. Coppola), wei_sun@hnu.edu.cn (W. Sun).

https://doi.org/10.1016/j.compbiomed.2019.103352
Received 8 May 2019; Received in revised form 7 July 2019; Accepted 7 July 2019
0010-4825/

In general, existing RVS approaches can be categorized as either supervised or unsupervised methods. The unsupervised segmentation method uses a system that segments retinal vessels without annotated, classified or labelled data. Conversely, the supervised or semi-supervised method uses labelled data.

The unsupervised methods mainly include strategies of matched filter responses, vessel tracking and prior experienced model-based approaches. Matched filter response techniques use the multi-scale kernel to conduct convolutional operations on retinal fundus images. They are used to determine the vessel locations using threshold techniques. Azzopardi et al. [4] proposed the B-COSFIRE method to obtain the selective responses of vessels' structure and obtained binary results by averaging the responses of the B-COSFIRE filters. The approach based on matched filtering techniques performs well on healthy images, but it is insufficient for pathological images [6]. Vessel tracking algorithms only improved the accuracy of the RVS by focusing on the local details of vessels. It could provide highly accurate vessel widths, but it cannot segment the retinal vessels without seed points. The prior experiences of retinal vessels were introduced to extract retinal vessels. Staal et al. [7] introduced centerlines to formulate the ridge-based method for the RVS. Lam et al. [8] used the shape prior of the vessel location. It considered the intensity of the vessel cross section as the Gaussian shape to improve the segmentation performance for low quality images. Other models, such as deformable models [9,10], were also proposed for the RVS.

Many supervised methods describe the segmentation as a pixel classification problem in which various visual features are extracted to train a powerful classifier that can distinguish the vessel and non-vessel pixels. These methods require the manual annotation of training data to learn how to extract vessels. Generally, supervised methods perform better than unsupervised methods [6].

Supervised methods commonly use machine learning algorithms, such as the SVM [11], Adaboost [12], or ANN [13] as the classifier. Fraz et al. [12] applied the Gabor filter response and orientation analysis of the gradient vector to extract multi-dimensional features and employed an ensemble learning method using Adaboost to train these features for the RVS. Marin et al. proposed an ANN-based supervised method. A representative 7-dimensional feature was built by combining grey-level and time-invariant features to train a multi-layer ANN for the RVS. In addition, Cheng et al. [14] adopted an RF to segment the mixed features of the contextual awareness that were obtained by various pre-processing algorithms.

Recently, Deep Learning (DL) has attracted great interest in the retinal imaging research community because of its strong ability to capture the information of higher semantic features, which makes the DL models outperform existing methods. Li et al. [15] remodeled the RVS task as a cross-modality transformation problem and trained a deep fully connected neural network using the G channel of colour retinal images without any pre-processing method. Liskowski et al. [16] first proposed a convolutional neural network (CNN) that was trained using a large amount of augmented data for the RVS. Dasgupta et al. [17] introduced a fully convolutional network to segment vessels, which was trained using the single G channel of the colour fundus image and the CLAHE algorithm. Wu et al. [18] designed a multi-scale network followed network (MS-NFN) with the cascade structure and four neural networks. The two first-level networks converted retinal images into probabilistic maps, and the two second-level networks refined the probabilistic maps. Many published supervised methods only used the G channel images to train their models [16–18], and obtained better performance compared with other methods using RGB colour retinal images.

In spite of the tremendous success of deep learning (DL) based methods, these algorithms still fail to precisely segment capillaries because of their small diameter and poor contrast of blood vessels in fundus images. When faced with extreme variations in the morphologies of the vessels against a noisy background, the single retinal vessel segmentation model, even based on DL, can hardly detect all the vessel details in the fundus images. Therefore, we propose a multi-proportional channel ensemble model to segment the vessels in fundus images. The model consists of five submodels, each of which are trained using the R and G channel composition data with different proportions and can detect different local vessel details. Finally, the retinal vascular probability maps that are generated by the five sub-models are averaged to obtain the refined segmentation results. The main contributions of this work include the following. (1) A novel ensemble model based on multi-proportional R and G channels is proposed, and it outperforms other existing methods with respect to two major performance metrics, i.e., the segmentation accuracy and the area under the Receiver Operating Characteristic (ROC) curve (AUC). (2) To the best of our knowledge, this report is the first to show that the red channel also produces performance gains for the RVS.

The remainder of our work is organized as follows. The details of the 4 datasets are described in Section 2. We presented a novel approach based on the MPC-EM in Section 3. The data preparation process is described and the robustness of the approach is assessed by experiments in Section 4. Finally, the discussion and conclusion are given in Section 5.

2. Materials

The proposed method is evaluated using four authoritative and publicly available datasets, i.e., DRIVE, STARE, CHASE_DB1, and HRF, which are regarded as the most popular datasets [6].

The DRIVE [7] dataset comes from the Netherlands-initiated DR screening project. It contains 40 fundus retinal images with a size of 584 × 565 pixels, and is averagely divided into training and testing datasets. Forty images are randomly selected from 400 diabetic subjects with 33 normal images and 7 images that showed symptoms of early DR. Each image is assigned a binary field of view (FOV) mask and ground-truth (GT) according to the manual annotations of independent experts.

The STARE dataset is comprised of 20 605 × 705 pixels fundus images with 8 bits per colour channel. The first ten images are pathological images and the rest of them are healthy images. Two observers annotated all of the images, and the performance is usually evaluated by the first observer's manual segmentation (the gold standard annotation) [4,12]. Because the training and testing data in the dataset are not divided by the author, we evaluate the performance using the leave one-out cross validation, as many other works [7,15,25] have done.

The CHASE_DB1 (Child Heart and Health Study in British) database is a subset of retinal images of multi-ethnic children. It consists of 28 images (960 × 996 pixels). Usually, the first 20 images are used for training, and the remaining 8 images are used for testing [15,18]. Compared with the DRIVE and STARE datasets, the CHASE_DB1 images have uneven background illumination, low contrast and broader arterioles [16].

The HRF dataset has 45 images (3304 × 2336 pixels), including 15 healthy images, 15 DR images and 15 glaucoma images. The FOV mask and ground truth segmentation for each image are produced by a group of experts. The dataset is not manually partitioned. Therefore, we evaluated the proposed method using the dataset as the method introduced in Ref. [26].

Because the STARE and CHASE_BD1 datasets have no FOV mask, a manual method [4,18,25] is used to get the FOV mask. Fig. 1 shows examples of the initial images, FOV masks, and ground truths from the DRIVE, STARE, CHASE_BD1, and HRF datasets, respectively.

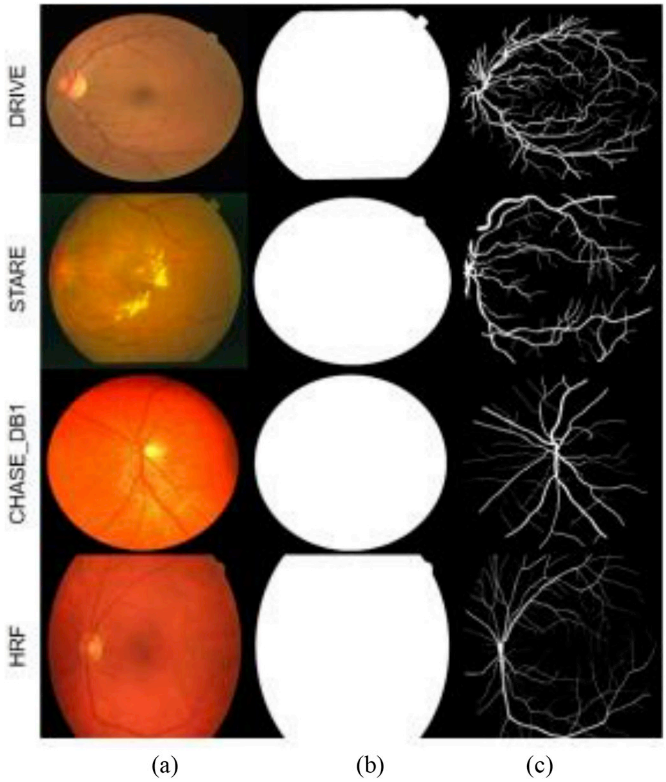

Fig. 1. Example of initial images (a), FOV masks (b) and ground truths (c).

3. Proposed method

3.1. MPC-EM structure

1) *Overall structure of the MPC-EM:* To simplify the model structure, we define the submodel that is trained with the αG-channel and (1-α)R-channel composition data as the αG + (1-α)R submodel. The proposed ensemble model (as shown in Fig. 2) has five submodels, i.e., the 0.6G + 0.4R, 0.7G + 0.3R, 0.8G + 0.2R, 0.9G + 0.1R, and G

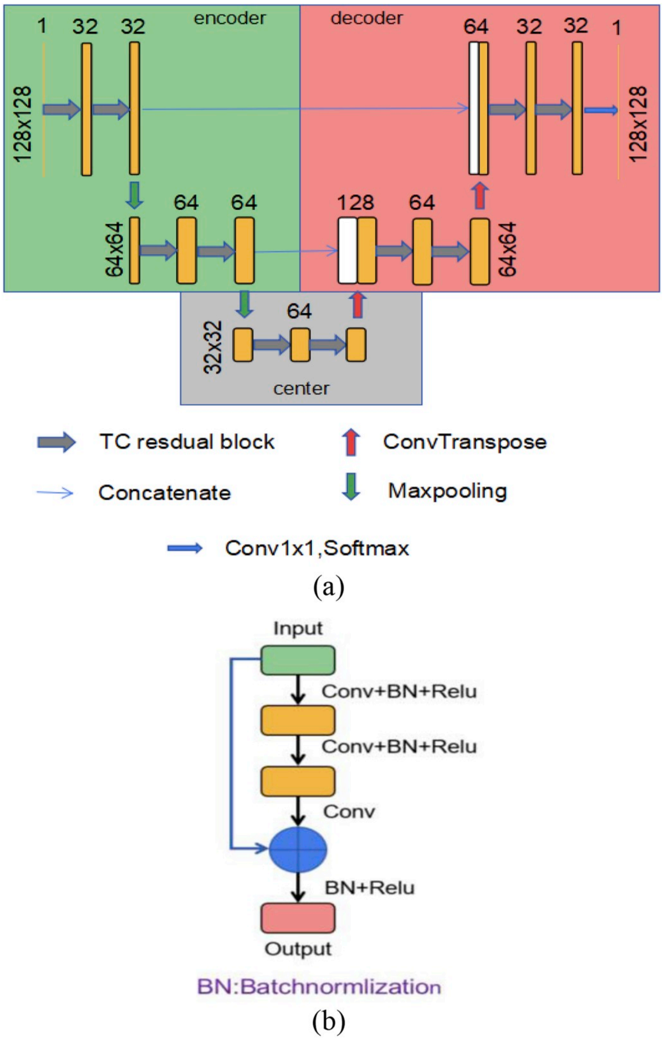

Fig. 3. Illustration of the proposed submodel structure: (a) submodel structure, and (b) illustration of the TC residual block.

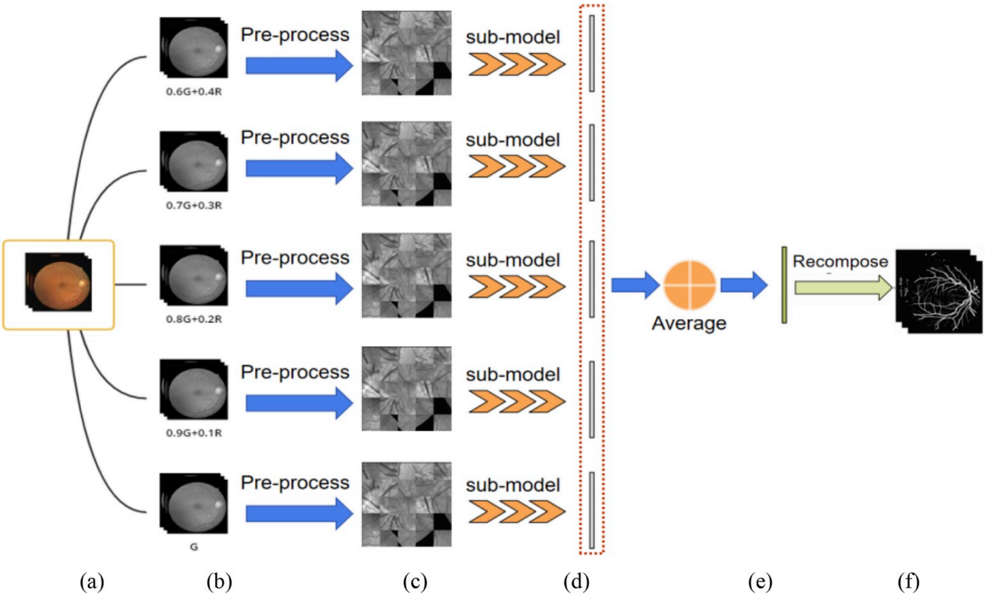

Fig. 2. Illustration of the MPC-EM based retinal vessel segmentation: (a) colour fundus image; (b) R-G channel composition image with different proportions; (c) preprocessed extraction image patches; (d) probabilistic maps of image patches produced by submodels; (e) probabilistic maps of image patches produced by the MPC-EM; (f) probabilistic maps produced by reconstruction of image patches. (For interpretation of the references to colour in this figure legend, the reader is referred to the Web version of this article.)

submodels, and each of them can detect different local details of fundus images. We propose the MPC-EM structure to improve the segmentation accuracy of retinal vessels mainly based on two points. (1) A single model, even based on deep learning, cannot segment all the vessels in the fundus images, particularly for the capillaries. (2) We discover that different proportional R and G channel composition images can provide us with different and useful global contrast and local vessel details. For the CHASE_DB1 and HRF datasets, there are clear differences between the 0.6G + 0.4R composition images and G images. For the DRIVE and STARE datasets, we cannot see the obvious differences in individual pictures, but the neural-network based submodel is sensitive to the global features of the whole dataset. Due to the different and useful features of the data that are input into each submodel, when using the backpropagation algorithm for optimization, the direction of optimization for each submodel will be different so that different local vessel details can be detected. The G-channel has been proved to be the most useful channel for RVG [19,20], while the blue channel (B channel) appears to be very weak and does not contain much information [19,20]. Therefore, we remove the B channel and set the ratio of the G channel to be greater than that of the R channel in all submodels. The interval is set to 0.1 and is used to ensure that each submodel learns different features.

2) *Submodel structure:* Each submodel, as shown in Fig. 3, has the U-Net-liked structure of encoder-center-decoder. The encoder part uses the convolutional, maxpooling, and ReLU [39] layers to convert the RGB images into the representational feature vectors. The decoder part mainly uses the ConvTranpose, convolutional and ReLU layers to converts the feature vectors into the probabilistic map. The ReLU reinforces the non-linear mapping ability of the network and accelerates the convergence speed of the model [39]. The center part is used as a transitional region to adjust the shape of feature vectors. This structure jointly uses the shallow localization information and higher semantic information to classify each pixel in images [27]. We set the triple convolutional (TC) residual block (see Fig. 2) as the basic block, which makes the whole network structure easier to optimize and avoid the vanishing gradient problem [37]. A batch normalization [21] (BN) layer is introduced to reduce the redundant parameters, and accelerate the deep network training.

3.2. Training details

The extracted patches with different proportions are fed into the five submodels that contain the same structure and preprocessing algorithms for independent training. The training mainly includes two stages. (1) In the forward-propagated phase, the difference between the labelled and predicted value is calculated by feeding image data into the model. (2) In the backward-propagated phase, the gradient descent algorithm is used to update the model parameters for minimizing the difference. The mini-batch adaptive moment estimation (mini-batch Adam [24]) algorithm is used to optimize the sub-model. The maximum number of iterations is set as 15, and 10000 images (128 × 128 pixels) that are randomly selected from the dataset are used to train the submodel in each epoch. The learning rate is initially set to 0.001 using the cosine annealing decreasing schedule. More comprehensible descriptions of deep learning and deep CNNs can be found in Refs. [22,23].

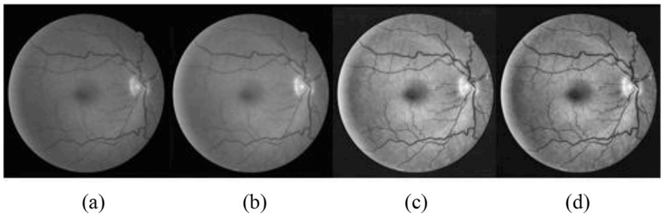
(a) (b) (c) (d)

Fig. 5. Visualization examples of the pre-processing algorithms. (a) G channel image data; (b) G channel image data with global normalization; (c) G channel image data with global normalization and CLAHE; (d) G channel image data with global normalization, CLAHE and gamma adjustment.

4. Data preparation

The R-G channel image data with different proportions are subject to the same image preprocessing and patch extraction, as shown in Fig. 4.

4.1. Image preprocessing

Before the raw image data was fed into the deep learning framework, proper preprocessing is always performed to obtain better segmentation and accelerate the training.

First, since the brightness may vary across the FOV [16], we perform global normalization by the following function.

$$I = (I - \alpha)/\lambda \qquad (1)$$

where I is one of the five proportions of R-G channel image data. α and λ denote the mean and standard deviation of the whole dataset, respectively.

Second, the CLAHE [20] is applied to boost the contrast between nonvessel and vessel. Finally, the gamma adjustment is used to reduce the background noise and improve the image quality. Fig. 5 shows some examples of the above algorithms.

4.2. Extraction of patch

Small image patches training has proved its superiority in many DL-based methods [15]— [18] by reducing the computational complexity during training and ensuring that local vessel details can be learned by

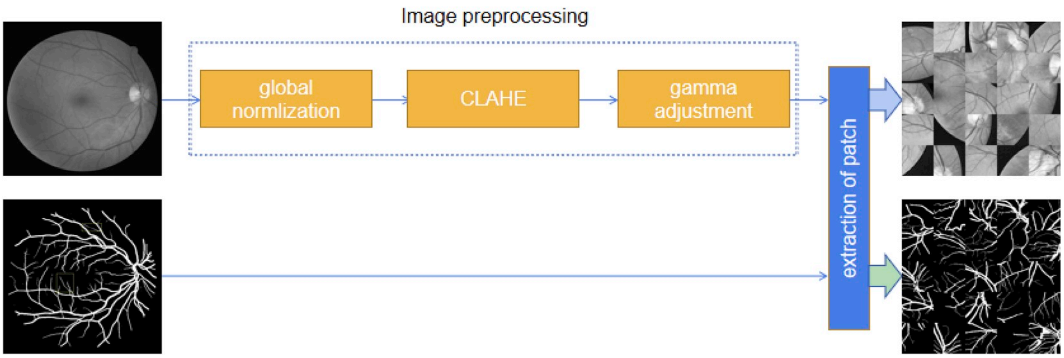

Fig. 4. Illustration of data preparation, which includes two step: (1) image preprocessing on the original image. (2) Patches extraction on both raw image and ground truth.

Table 1
Measures for segmentation results.

	ground truth = vessel	ground truth = non-vessel
segmentation result = vessel	*TP*	*FP*
segmentation result = non-vessel	*FN*	*TN*

submodel. In this work, 128 × 128 × 3 image patches are extracted with 32 pixels per step, this results in 225 image patches per original image, 4500 image training patches, and 4500 image testing patches for the DRIVE dataset, in addition to 775 image patches per original image, 15500 training image patches, and 6200 testing image patches for the CHASE_DB1 dataset. Because the STARE dataset has not been divided into training and testing datasets, we get 775 image patches per image and 6000 image patches from the whole dataset and use the *leave-one-out* method [15] to evaluate the proposed method. 30000 training image patches and 12000 image patches are obtained using the above method on the HRG dataset.

5. Experimental evaluation

We described a great quantity of experimental results in this Section, and compares the existing methods with the proposed method. Section 5.1 describes the evaluation metrics. Section 5.2 presents the results and comparisons between all the submodels and the MPC-EM.

5.1. Evaluation metric

The RVS result can be divided into two categories: vessel (positive) and nonvessel (negative). By validating the RVS results with manual annotations (gold standard), 4 measures can be obtained and presented in Table 1, i.e., true positives (*TP*), false negatives (*FN*), true negatives (*TN*), and false positives (*FP*).

Four performance criteria are used to compare the proposed MPC-EM based approach with other SOTA methods, i.e., the sensitivity (*SE*), specificity (*SP*), accuracy (*ACC*) and area under the ROC curve (*AUC*). All the metrics are calculated only for the pixels inside the FOV (the pixels in the white part of FOV mask in Fig. 1). These metrics can be illustrated as follows,

$$SE = \frac{TP}{TP + FN}$$

$$SP = \frac{TN}{TN + FP}$$

$$ACC = \frac{TP + FN}{TP + FN + TN + FP}$$

$$MCC = \frac{TP/N - S \times P}{\sqrt{P \times S \times (1 - S) \times (1 - P)}}$$

where $N = TP + TN + FP + FN$, $S = (TP + FN)/N$, and $P = (TP + FP)/N$.

The outcome of the proposed MPC-EM or submodel is a vessel probabilistic map in which each value corresponds to the confidence that each pixel is a vessel or non-vessel. The ROC curve is produced by changing the threshold, and the AUC is obtained using the *scikit-learn* Python library in our experiments.

5.2. Experimental results

To prove the generality of the MPC-EM framework and submodels, we also apply the U-Net [27] as a submodel, which is the base structure of many excellent segmentation algorithms. To describe the relationship between the submodel and MPC-EM framework, we presented results of the five submodels (the designed submodel and the U-Net, respectively) and the MPC-EM for the DRIVE, STARE, CHASE_DB1, and HRF datasets. In addition, the cross-training method evaluates the capability of the MPC-EM for the RVS without using specific training datasets, which has proven its robustness under the realistic situation.

Table 2
Performance measures for the DRIVE, STARE, AND CHASE_DB1 datasets.

Dataset	Method	AUC (%)	ACC (%)	SE (%)	SP (%)
DRIVE	Proposed method	98.22	95.74	85.64	97.10
	2nd Human Observer	–	94.72	77.60	97.24
STARE	Proposed method	98.98	96.95	81.62	98.69
	2nd Human Observer	–	93.49	89.52	93.84
CHASE_BD1	Proposed method	98.50	96.54	81.06	98.07
	2nd Human Observer	–	95.45	81.05	97.11
HRF	Proposed method	98.43	96.31	77.82	98.43

1) *Vessel Segmentation:* In the following part, all experimental results are obtained using the designed submodel (see Fig. 3). The five submodels and MPC-EM binary segmentation results are obtained by selecting a threshold of 0.5 on those produced probabilistic maps. Pixels with a probability greater than 0.5 are considered to be positive (vessel); otherwise, they are negative (nonvessel). These probabilistic maps are used to calculate the AUC, and the segmentation results are used to calculate the ACC, SE, and SP. The evaluation metrics of our method for the abovementioned datasets are shown in Table 2. Fig. 6 shows the visualization examples of the RVS results and the zoomed details of the 0.6G + 0.4R submodel, the G submodel and the MPC-EM on the DRIVE dataset; the RVS results for the remaining 3 datasets are displayed in Figs. 7-9, respectively.
    1) *Comparison of the submodel and MPC-EM*: The performance of the five submodels (based on both U-Net and the designed structure) and the MPC-EM are shown in Tables 3–6, respectively. In general, the MPC-EM performs better with respect to the AUC and accuracy than the G submodel, regardless of whether it is based on U-Net or the designed submodel. The AUC and accuracy of MPC-EM on the DRIVE dataset are 98.22% and 95.74%, respectively, and the values for the G submodel are 97.81% and 95.58%, respectively. For the CHASE_DB1 dataset, the AUC and accuracy of the MPC-EM are 98.50% and 96.54%, respectively, and those for the G submodel are 98.26% and 96.29%, respectively. For the STARE dataset, the leave-one-out [7] approach is used to evaluate the proposed method. The AUC and accuracy of the G submodel are 98.63% and 96.76%, respectively, and the values of the MPC-EM are 96.98% and 96.95%, respectively. From Tables 3–6, one can obtain that the G submodel is not the most effective model for all datasets. On the DRIVE dataset, the 0.7G + 0.3R submodel obtains a better AUC than the G submodel.
    2) *Comparison with other SOTA methods*: The performances of the MPC-EM are compared with the SOTA methods in Tables 7–10, respectively. In summary, our method achieved better sensitivity and accuracy, especially the improvement in the sensitivity compared with the second best performing method. The AUC values of the proposed method are 98.22%, 98.98% and 98.50%, respectively. The AUCs are higher than the existing method on the DRIVE and CHASE_BD1 datasets and slightly lower than the method from Ref. [16] on the STARE dataset. A detailed analysis of the experimental results is presented in Section 6.
    3) *Cross-Training and Pathological Image:* The robustness of the proposed method in different realistic situations is verified using cross-training method [16]. From Table 13, it is notable that the MPC-EM achieves better AUC and ACC in the cross-training compared with other algorithms. We also present the performance metrics of the pathological images from the STARE

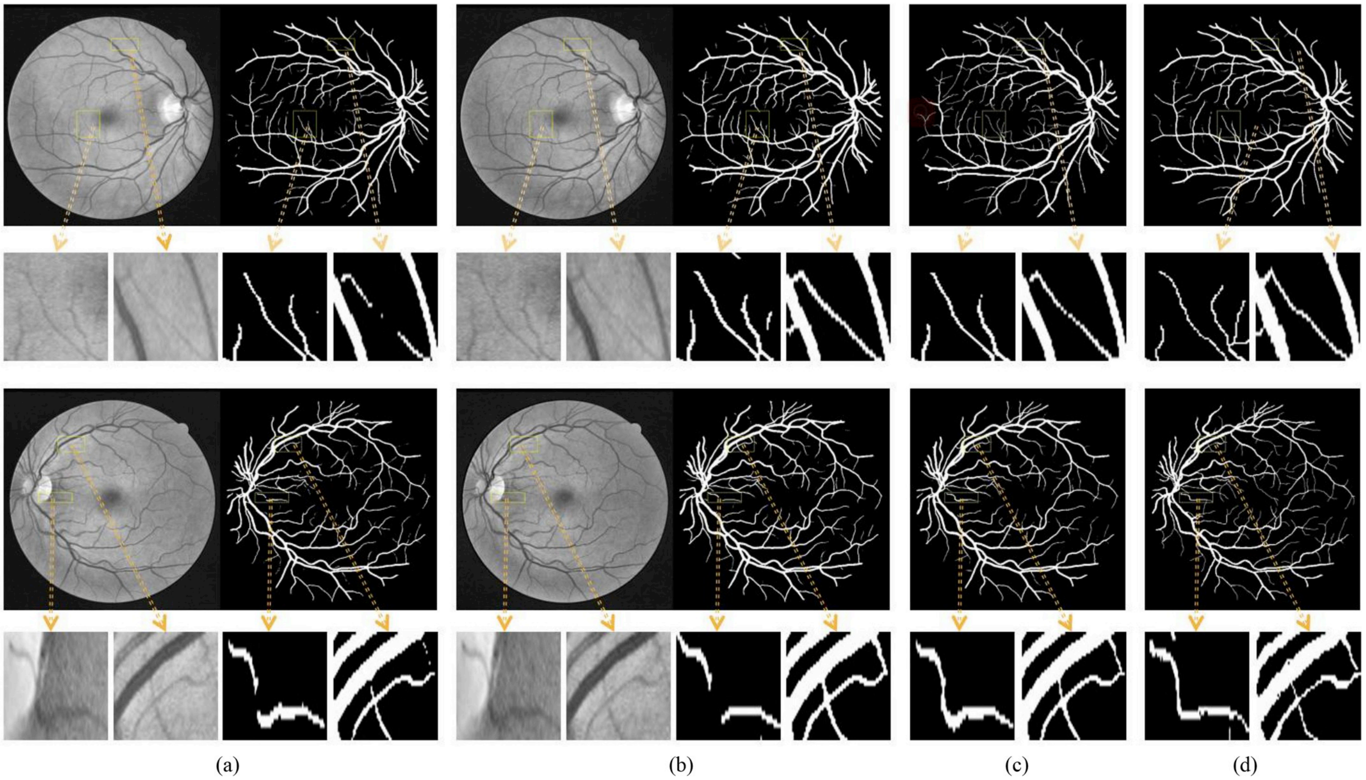

Fig. 6. Segmentation results (the 1st and 3rd rows) and their zoomed details (the 2nd and 4th rows) for the DRIVE dataset: (a) 0.6G + 0.4R submodel segmentation results: preprocessed images (left) and binary segmentation result (right); (b) G submodel segmentation results: preprocessed images (left) and binary segmentation results (right); (c) MPC-EM segmentation results; and (d) the ground truth.

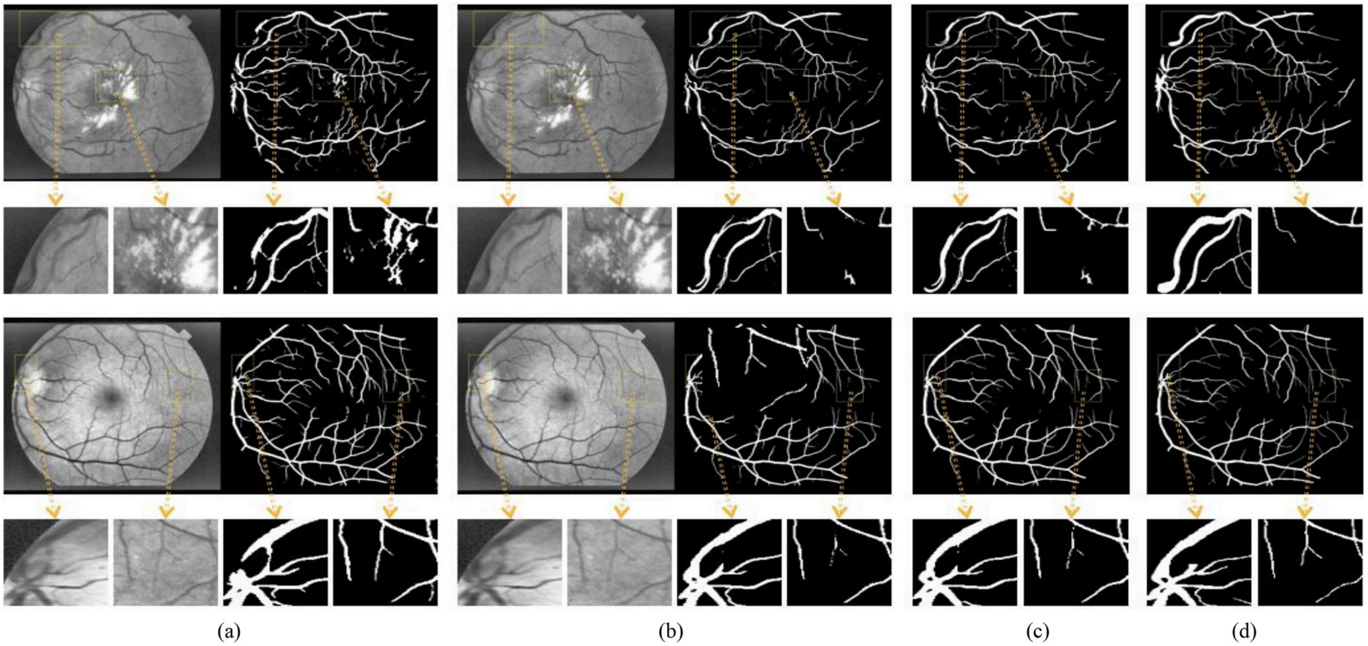

Fig. 7. Segmentation results (the 1st and 3rd rows) and their zoomed details (the 2nd and 4th rows) for the STARE dataset: (a) 0.6G + 0.4R submodel segmentation results: preprocessed images (left) and binary segmentation results (right); (b) G submodel segmentation results: preprocessed images (left) and binary segmentation results (right): (c) MPC-EM segmentation results; and (d) the ground truth.

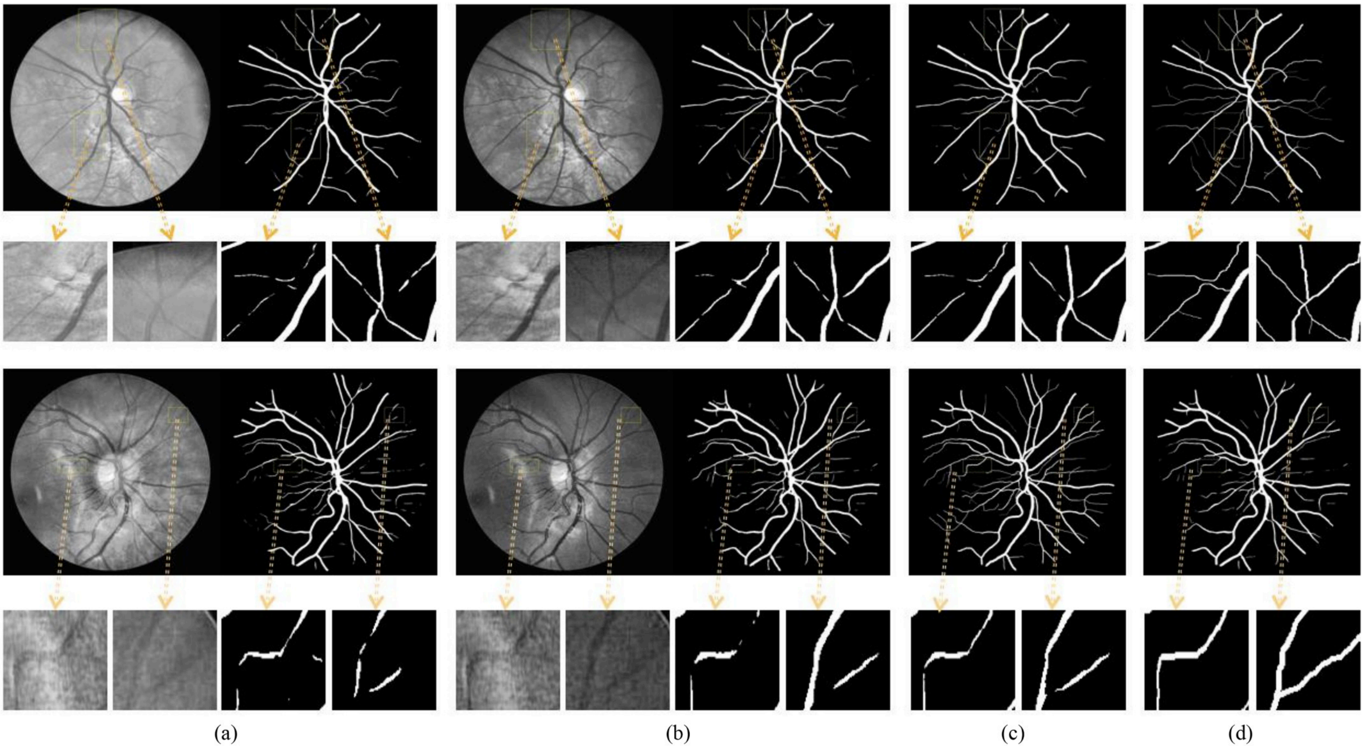

Fig. 8. Segmentation results (the 1st and 3rd rows) and their zoomed details (the 2nd and 4th rows) for the CHASE_BD1 dataset: (a) 0.6G + 0.4R submodel segmentation results: preprocessed images (left) and binary segmentation results (right); (b) G submodel segmentation results: preprocessed images (left) and binary segmentation results (right); (c) MPC-EM segmentation results; and (d) the ground truth.

dataset in Table 12 to verify of its ability to help the diagnosis process.

6. Discussion and conclusion

In this work, we presented a novel supervised method based on the MPC-EM framework for the RVS in fundus images. The MPC-EM comprises five submodels, each of which is trained using the proportional composition of the R-G channel images with identical pre-processing algorithms and can detect different local vessel details of fundus images. Submodels convert the different R-G channel composed images into probabilistic maps, and these maps are averaged into a refined segmentation result. The MPC-EM framework is able to take full advantage of the useful feature information of fundus images and performs better with reduced computational complexity.

When considering the performance metrics of the AUC, accuracy, sensitivity, and specificity, the proposed MPC-EM framework outperforms other SOTA methods on the DRIVE, STARE and CHASE_DB1 datasets. The ACCs that are obtained by the proposed method on the datasets are 95.74%, 96.95%, 96.31%, and 96.54%, respectively, which

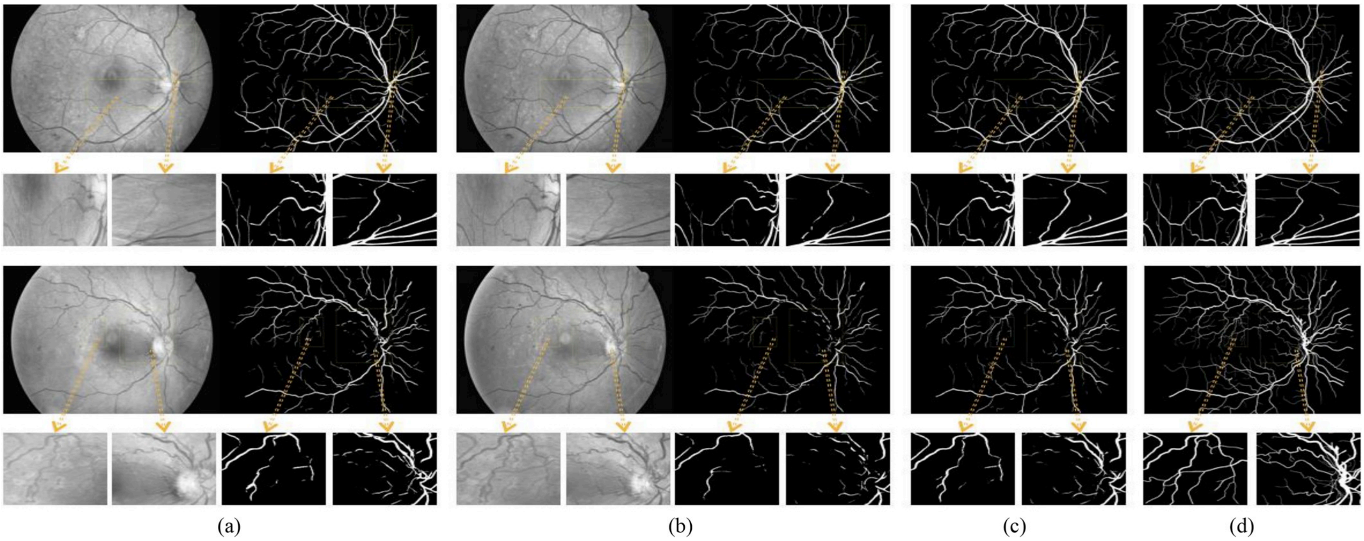

Fig. 9. Segmentation results (the 1st and 3rd rows) and their zoomed details (the 2nd and 4th rows) for the HRF dataset: (a) 0.6G + 0.4R submodel segmentation results: preprocessed images (left) and binary segmentation results (right); (b) G submodel segmentation results: preprocessed images (left) and binary segmentation results (right); (c) MPC-EM segmentation results; and (d) the ground truth.

Table 3
Performance using the DRIVE dataset.

	AUC (%)	ACC (%)	SE (%)	SP (%)
0.6G + 0.4R(U-Net)	97.81	95.51	78.94	97.93
0.7G + 0.3R(U-Net)	97.83	95.52	79.76	97.81
0.8G + 0.2R(U-Net)	97.77	95.49	79.35	97.85
0.9G + 0.1R(U-Net)	97.81	95.51	76.34	**98.31**
G(U-Net)	97.75	95.53	78.92	97.95
MPC-EM(U-Net)	98.12	95.67	78.98	98.09
0.6G + 0.4R	97.95	95.55	**81.83**	97.55
0.7G + 0.3R	97.96	95.58	79.77	97.89
0.8G + 0.2R	97.84	95.57	80.40	97.82
0.9G + 0.1R	97.84	95.65	78.76	98.11
G	97.81	95.58	78.94	98.01
MPC-EM	**98.22**	**95.74**	80.83	97.90

Table 4
Performance using the STARE dataset.

	AUC (%)	ACC (%)	SE (%)	SP (%)
0.6G + 0.4R(U-Net)	97.90	96.37	77.53	98.51
0.7G + 0.3R(U-Net)	97.84	96.38	76.63	98.62
0.8G + 0.2R(U-Net)	98.37	96.60	79.67	98.52
0.9G + 0.1R(U-Net)	98.33	96.65	79.88	98.56
G(U-Net)	98.38	96.64	80.53	98.47
MPC-EM(U-Net)	98.73	96.79	79.96	98.68
0.6G + 0.4R	98.34	96.43	78.53.	98.55
0.7G + 0.3R	98.26	96.61	79.00	98.61
0.8G + 0.2R	98.50	96.73	79.61	98.67
0.9G + 0.1R	98.44	96.74	80.15	98.62
G	98.63	96.76	80.56	98.60
MPC-EM	**98.98**	**96.95**	**81.62**	**98.69**

Table 5
Performance using the CHASE_BD1 dataset.

	AUC (%)	ACC (%)	SE (%)	SP (%)
0.6G + 0.4R(U-Net)	97.46	96.08	70.63	**98.61**
0.7G + 0.3R(U-Net)	97.71	96.28	75.86	98.32
0.8G + 0.2R(U-Net)	97.82	96.14	80.50	97.69
0.9G + 0.1R(U-Net)	98.03	96.27	81.05	97.79
G(U-Net)	97.95	96.13	80.89	97.65
MPC-EM(U-Net)	98.29	96.45	78.55	98.23
0.6G + 0.4R	98.07	96.35	80.84	97.89
0.7G + 0.3R	98.00	96.33	78.02	98.15
0.8G + 0.2R	98.13	96.44	78.95	98.18
0.9G + 0.1R	98.05	96.31	79.72	97.96
G	98.16	96.38	80.35	97.98
MPC-EM	**98.50**	**96.54**	**81.38**	98.06

Table 6
Performance using the HRF dataset.

	AUC (%)	ACC (%)	SE (%)	SP (%)
0.6G + 0.4R(U-Net)	97.28	95.88	76.53	98.74
0.7G + 0.3R(U-Net)	97.78	96.10	75.22	98.58
0.8G + 0.2R(U-Net)	97.84	96.03	74.00	98.66
0.9G + 0.1R(U-Net)	97.94	96.03	74.35	98.61
G(U-Net)	97.98	96.16	76.63	98.49
MPC-EM(U-Net)	98.25	96.18	74.69	98.73
0.6G + 0.4R	97.66	96.08	76.77	98.38
0.7G + 0.3R	97.86	95.99	71.47	**98.91**
0.8G + 0.2R	98.10	96.20	75.81	98.63
0.9G + 0.1R	98.08	96.23	77.66	98.45
G	98.15	96.23	**77.82**	98.43
MPC-EM	**98.43**	**96.31**	76.53	98.66

are better than the existing SOTA methods. The improvement of the ACC mainly results from the substantial increase of the sensitivity, which reflects the ability to detect the vessels. The SEs that are obtained by the proposed method for the above three datasets are 80.83%, 81.62%, and 81.38%, respectively (i.e., it is 2.39% higher than the second best SE result for the DRIVE and 6.00% higher than the second best method for the CHASE -DB1). These results prove the strong ability of our method to detect the vessel details.

When considering the performance metrics of the AUC, accuracy, sensitivity, and specificity, the proposed MPC-EM method outperforms other SOTA methods on the DRIVE, STARE, and CHASE_DB1 datasets. The ACCs that are obtained by the proposed method on the datasets are 95.74%, 96.95%, 96.31%, and 96.54%, respectively, which are better than the existing SOTA methods. The improvement of the ACC mainly results from the substantial increase of the sensitivity, which reflects the ability to detect the vessels. The SEs that are obtained by the proposed method on the three datasets are 80.83%, 81.62%, and 81.38%, respectively (i.e., 2.39% higher than the second best SE result on the DRIVE and 6.00% higher than the second best method for the CHASE -DB1). These results prove the strong ability of our method to detect the vessel details.

Due to the characteristics of fundus images, almost all existing methods for RVS are based on raw images or the G channel, and the G channel based models generally perform better than raw image models. In this work, we find that the R channel of colour fundus images is also able to improve the performance using the proposed approach. From Tables 3–5, one can see that the AUC and ACC with single the G channel submodel are 97.81% and 95.58% on the DRIVE dataset, respectively.

The AUC and ACC values are 98.62% and 96.25% on the STARE dataset, 98.26% and 96.29% on the CHASED_DB1 dataset, and 98.15% and 96.23% on the HRF dataset, respectively. Compared with the G submodel, the AUC and ACC with the MPC-EM are improved to 98.22% and 95.74% on the DRIVE dataset. These values are 98.50% and 96.95% on the STARE dataset, 98.50% and 96.54% on the CHASED_DB1 dataset, and 98.43% and 96.31% on the HRF dataset, respectively. The comparisons between the five submodels show that the G submodel performs the best on the STARE and CHASE_DB1 datasets and the 0.7G + 0.3R submodel performs the best on the DRIVE dataset. Those results prove that the R channel can also generate a better performance to improve segmentation accuracy, and the MPC-EM can obtain a better segmentation performance than a single G model. The improvement that results from the MPC-EM, regardless of whether it is based on U-Net or the designed submodel, demonstrates that the MPC-EM method can be easily applied to many segmentation models and boost the models' performance. The results inform the cross-training (Table 13) illustrate that the proposed method has strong robustness when dealing with realistic situations. From the comparison with the results of the pathological retinal images from the STARE dataset (see Table 12), the MPC-EM obtained better ACC compared with the SOTA methods [13,15,16], which implies that our method can help doctors to better diagnose eye diseases and other complications. Compared with the SOTA methods, in addition to the improvement of the segmentation accuracy, our method also reduces the inference time. The average time to process a 580 × 565 retinal image is less than 5 s (Table 11). The reduction of the inference time comes mainly for two reasons. (1) Compared with the existing methods ([4,13,30], and [31]) that do not use GPUs, we used a GPU to accelerate the training and testing. (2) Compared to the methods with GPUs [18], the reduction of the time mainly results from the extraction of the partly overlapped patches (See Section 4.2). In Ref. [18], 48 × 48 image patches are extracted in an orderly manner with a step size of 32 pixels, thus resulting in approximately 8200 image patches per original image of the DRIVE dataset, and those heavily overlapped predictions are used to detect more vessel details. In the proposed method, we set the patch size to 128 × 128 and the stride is 32 pixels to extract 225 image patches for an original image from DRIVE. All experiments in this work are conducted on the computer with an i7-7700 3.60 GHz CPU and a single GeForce GTX 1080TI GPU. The MPC-EM is implemented using Keras 2.1.5. The average training time is less than 3 h for the MPC-EM and a

Table 7
Performance Comparison with respect to other existing methods on the drive.

Type	Methods	Year	AUC (%)	ACC (%)	SE (%)	SP (%)	MCC(%)
Unsupervised Methods	Zana et al. [28]	2001	89.84	93.77	69.71	N.A.	–
	Jiang et al. [29]	2003	91.14	92.12	N.A.	N.A.	–
	Mendonca et al. [30]	2006	N.A.	94.40	69.96	97.30	–
	Al-Diri et al. [31]	2009	N.A.	N.A.	72.82	95.51	–
	Lam et al. [32]	2010	96.14	94.72	N.A.	N.A.	–
	Fraz et al. [6]	2011	N.A.	94.30	71.52	97.95	–
	Azopardi et al. [4]	2015	96.14	94.42	76.55	97.04	–
	Mapayi et al. [34]	2015	97.11	95.00	74.06	98.07	–
Supervised Methods	Niemeijer et al. [35]	2004	92.94	94.16	N.A.	N.A.	–
	Staal et al. [7]	2004	96.14	94.61	73.32	97.82	
	Soare et al. [25]	2006	95.20	94.41	N.A.	N.A.	–
	Fraz et al. [13]	2012	97.47	94.80	74.06	98.07	
	Cheng et al. [14]	2014	96.48	94.74	72.52	97.98	
	Li et al. [15]	2015	97.38	95.27	75.69	98.16	–
	Liskowski et al. [16]	2016	97.91	95.35	78.11	98.07	–
	Orlando et al. [26]	2017	–	–	78.74	95.84	75.56
	Dasgupta et al. [17]	2017	97.44	95.33	76.91	98.01	–
	Wu et al. [18]	2018	98.07	95.67	78.44	98.19	–
	MPC-EM	**2019**	**98.22**	**95.74**	**80.83**	**97.96**	**79.84**

Table 8
Performance comparison with respect to other existing methods on the STARE.

Type	Methods	Year	AUC (%)	ACC (%)	SE (%)	SP (%)	MCC(%)
Unsupervised Methods	Mendonca et al. [30]	2006	N.A.	94.40	69.96	97.30	–
	Al-Diri et al. [31]	2009	N.A.	N.A.	75.21	96.81	–
	Lam et al. [32]	2010	97.39	95.67	N.A.	N.A.	–
	Fraz et al. [6]	2011	N.A.	94.42	73.11	96.80	–
	Azzopardi et al. [4]	2011	94.97	95.63	77.16	97.01	–
	Mapayi et al. [34]	2015	N.A.	95.10	76.26	96.57	–
Supervised methods	Staal et al. [7]	2004	96.14	95.16	N.A.	N.A.	–
	Soares et al. [25]	2006	96.71	94.79	72.07	97.47	–
	Fraz et al. [13]	2012	97.68	95.34	75.48	97.63	–
	Li et al. [15]	2015	98.79	96.28	77.26	98.44	–
	Orlando et al. [26]	2017	–	–	78.74	95.84	74.17
	Liskowski et al. [16]	2016	99.30	96.67	92.89	97.10	–
	MPC-EM	**2019**	**98.98**	**96.95**	**81.62**	**98.69**	**80.66**

Table 9
Performance comparison with respect to other existing methods on the HRF.

Type	Methods	Year	AUC (%)	ACC (%)	SE (%)	SP (%)	MCC(%)
Supervised method	Odstrcilik et al. [37]	2013	–	–	77.94	96.50	–
	Orlando et al. [26]	2017	–	–	78.74	95.84	70.46
	MPC-EM	**2019**	**98.43**	**96.31**	**77.82**	**98.43**	**77.00**

Table 10
Performance comparison with SOTA method on the CHASE_DB1.

Type	Methods	Year	AUC (%)	ACC (%)	SE (%)	SP (%)	MCC(%)
Unsupervised method	Azzopardi et al. [4]	2015	94.87	93.81	75.85	95.87	–
Supervised method	Fraz et al. [13]	2012	97.12	94.69	72.24	97.11	–
	Li et al. [15]	2016	97.16	95.81	75.07	97.93	–
	Orlando et al. [26]	2017	–	N.A.	72.77	97.12	70.65
	Wu et al. [18]	2018	98.25	96.37	75.38	98.47	–
	MPC-EM	**2019**	**98.50**	**96.54**	**81.38**	**98.07**	**79.69**

half hour for each submodel for a single dataset.

Experiments about the ensemble of deep learners with combinations that included weighted versions of all R, G and B channels were conducted. As shown in Table 14, the MPC-EM-GR achieved almost same segmentation performance as the MPC-EM-ALL. However, the MPC-EM-ALL needs to ensemble 15 models while the MPC-EM-GR only needs 5 models. These results illustrate that the MPC-EM-GR has less parameters and computational complexity than the MPC-EM-ALL. These results also prove that most useful information of retinal vessel is contained in G and R channels.

Further experiments were carried out to discuss the effect of different patch sizes on the segmentation performance. The patch size over

Table 11
Performance comparison of the inference time.

Type	Method	Year	Time
Unsupervised methods	Mendonca [30]	2006	2.5 min
	Al-Diri [31]	2009	11 min
	Azzopardi [4]	2015	10 S
Supervised methods	Soares [25]	2006	3 min
	Fraz [13]	2012	2 min
	Li [15]	2015	1.2 min
	Wu [18]	2018	10 S
	MPC-EM	2019	5 S

Table 12
Performance comparison of pathological retinal images.

Method	AUC (%)	ACC (%)	SE (%)	SP (%)
Hoover [36]	–	92.58	65.87	95.56
Soares [25]	–	95.00	71.81	97.65
Fraz [13]	–	95.11	72.62	97.64
Li [15]	–	96.72	78.00	98.05
Liskowski [16]	99.12	96.41	91.95	96.90
MPC-EM	**98.99**	**97.06**	**81.62**	**98.82**

Table 13
Performance comparison of the cross-training.

Dataset	Method (tanning dataset)	AUC (%)	ACC (%)	SE (%)	SP (%)
DRIVE	[25](STARE)	–	93.97	–	–
	[24](STARE)]	–	92.66	–	–
	[16](STARE)]	–	94.48	–	–
	[13](STARE)	96.97	94.56	72.42	97.92
	[15](STARE)	96.77	94.86	72.73	98.10
	[16](STARE)	96.05	94.16	–	–
	MPC-EM (STARE)	**97.40**	**95.01**	**76.52**	**98.10**
STARE	[25](DRIVE)	–	93.27	–	–
	[24](DRIVE)	–	94.64	–	–
	[16](DRIVE)	–	95.28	–	–
	[13](DRIVE)	96.60	94.95	70.10	97.70
	[15](DRIVE)	96.71	95.45	70.24	98.28
	[16](DRIVE)	95.95	95.05	–	–
	MPC-EM (DRIVE)	**97.54**	**95.22**	**74.47**	**97.75**

Table 15
Effect of different patch size on segmentation performance using the proposed network structure on the Drive dataset.

patch size	G	R	AUC (%)	ACC (%)	SE (%)	SP (%)
32 × 32	1.0	0.0	97.77	95.48	78.85	97.88
	0.9	0.1	97.87	95.50	78.27	98.01
	0.8	0.2	97.79	95.47	77.42	98.11
	0.7	0.3	97.91	95.57	79.75	97.87
	0.6	0.4	97.82	95.52	78.37	98.02
	MPC-EM		98.04	95.60	78.70	98.06
64 × 64	1.0	0.0	97.81	95.54	77.78	98.13
	0.9	0.1	97.82	95.55	78.46	98.04
	0.8	0.2	97.81	77.63	98.03	95.51
	0.7	0.3	97.90	95.54	78.69	97.99
	0.6	0.4	97.91	95.60	76.83	98.29
	MPC-EM		98.11	95.65	77.51	**98.30**
128 × 128	1.0	0.0	97.95	95.55	**81.83**	97.55
	0.9	0.1	97.96	95.58	79.77	97.89
	0.8	0.2	97.84	95.57	80.40	97.82
	0.7	0.3	97.84	95.65	78.76	98.11
	0.6	0.4	97.81	95.58	78.94	98.01
	MPC-EM		**98.22**	**95.74**	80.83	97.90

Table 16
Effect of different colour spaces on segmentation performance using the proposed network on the DRIVE dataset.

Colour Spaces	AUC (%)	ACC (%)	SE (%)	SP (%)
RGB	97.82	95.55	**78.66**	98.01
HSV	97.80	95.53	79.66	97.84
LAB	97.79	95.55	77.23	98.22

256 × 256 would result in insufficient number of patches for the training, therefore, the maximum patch size is set to 128 × 128. As shown in Table 15, with the increase of patch size, the performance of the MPC-EM becomes better. The results show that the patch size of 128 × 128 is more suitable for the MPC-EM.

The relationship between RGB and other color space (e.g., HSV, LAB) is nonlinear, and the convolutional neural network (CNN) also has a strong ability of nonlinear feature mapping. Therefore, we think using alternative colour spaces to replace RGB should be similar in terms of segmentation performance, when using the CNN-based method. We also conducted an experiment to evaluate the effect of different colour spaces on segmentation performance. These experimental results, as shown in Table 16, also prove the presumption.

Table 14
The performance of MPC-EM of weighted versions of R, G, and B on the DRIVE dataset.

G	R	B	AUC (%)	ACC (%)	SE (%)	SP (%)	number of ensemble models
0.6	0.4	0.0	97.95	95.55	**81.83**	97.55	1
	0.3	0.1	97.82	95.59	78.27	98.17	
	0.2	0.2	97.85	95.57	77.26	98.19	
	0.1	0.3	97.83	95.55	77.90	98.12	
	0.0	0.4	97.80	95.55	78.25	98.12	
0.7	0.3	0.0	97.96	95.58	79.77	98.10	
	0.2	0.1	97.96	95.56	78.50	97.97	
	0.1	0.2	97.73	95.47	77.43	98.12	
	0.0	0.3	97.67	95.37	78.20	98.21	
0.8	0.2	0.0	97.84	95.57	80.40	97.82	
	0.1	0.1	97.85	95.54	77.23	98.20	
	0.0	0.2	97.80	95.50	76.74	98.17	
0.9	0.1	0.0	97.84	95.65	78.76	98.11	
	0.0	0.1	97.80	95.50	7674	98.17	
1	0.0	0.0	97.81	95.58	78.74	98.01	
MPC-EM-ALL			**98.24**	95.73	79.77	**98.25**	15
MPC-EM-GR (0.9G + 0.1R, 0.8G + 0.2R, 0.7R + 0.3R, 0.6G + 0.4R, G)			98.22	**95.74**	80.83	97.90	5

MPC-EM-ALL: ensemble of all models, MPC-EM-GR: ensemble of all the models except for models with b channels.

Table 17
Effect of Different Interval Ensemble on Segmentation Performance using the Proposed Network Structure on the DRIVE Dataset.

G	R	AUC (%)	ACC (%)	SE (%)	SP (%)	number of ensemble models
1.0	0.0	97.81	95.58	78.94	98.01	1
0.95	0.05	97.93	95.63	79.50	97.98	
0.9	0.1	97.84	95.65	78.76	98.11	
0.85	0.15	97.83	95.50	77.16	98.01	
0.8	0.2	97.84	95.57	80.40	97.82	
0.75	0.25	97.94	95.53	76.84	98.1 6	
0.7	0.3	97.96	95.58	79.77	97.89	
0.65	0.35	97.95	95.58	77.21	98.26	
0.6	0.4	97.95	95.55	**81.83**	97.55	
MPC-EM (interval = 0.05)		98.23	95.72	78.35	**98.26**	9
MPC-EM (interval = 0.1)		**98.22**	**95.74**	80.83	97.90	5

We conduct the experiments to evaluate the effect of different interval ensemble on segmentation performance. As shown in Table 17, compared with the ensemble with an interval of 0.05, the ensemble with an interval of 0.1 has almost the same segmentation performance but less computational complexity.

Deep learning has achieved excellent performance in the computer vision field, and it has also been proven to be successful in retinal vessel segmentation. However, many researchers only focus on the optimization of the structures of neural networks and ignore the design of manual features. Compared with the results of DL-based [15–17] models, we find that the model without preprocessing is not as good as that with pre-processing.

To the best of our knowledge, almost all the supervised methods can be divided into two categories: those trained using the G-channel of fundus images and those trained using raw images. In this paper, we propose a novel MPC-EM framework, which is trained using different proportions of the R and G channels. It performs better with reduced computational complexity than the existing methods that are trained using a single G-channel or raw images. In summary, we presented a new supervised method for the RVS, and the proposed MPC-EM approach proved that the R channel can also produce performance gains. This method has wide application prospects due to its high accuracy, strong robustness, and reduced computational complexity.

Funding

Manuscript received Jan. 17, 2019. This work was supported in part by the National Natural Science Foundation of China (NSFC 61673163), Chang-Zhu-Tan National Indigenous Innovation Demonstration Zone Project (2017XK2102), the Hunan Provincial Natural Science Foundation of China (2016JJ3045), and t Hunan Key Laboratory of Intelligent Robot Technology in Electronic Manufacturing (IRT2018003). (Corresponding author: Q. Liang).

Conflict of interest statement

None declared.

References

[1] M.D. Abrmoff, M.K. Garvin, M. Sonka, Retinal imaging and image analysis, IEEE Trans. Med. Imaging 3 (2010) 169–208.
[3] CDC, Diabetic Retinopathy. Atlanta, GA: National for Chronic Disease Prevention and Health Promotion [Online], (2011, Mar) Available: http://www.cdc.gov/visionhealth/pdf/factsheet.pdf.
[4] G. Azzopardi, N. Strisciuglio, M. Vento, N. Petkov, Trainable COSFIRE filters for vessel delineation with application to retinal images, Med. Image Anal. 19 (Feb. 2015) 46–57.
[5] C. Kirbas, F. Quek, A review of vessel extraction techniques and algorithms, ACM Comput. Surv. 36 (Jun. 2004) 81–121.
[6] M.M. Fraz, et al., "Blood vessel segmentation methodologies in retinal images—a survey, Comput. Methods Progr. Biomed. 108 (1) (2012) 407–433.
[7] J. Staal, M.D. Abramoff, M. Niemeijer, M.A. Viergever, B. Van Ginneken, Ridge-based vessel segmentation in color images of the retina, IEEE Trans. Med. Imaging 23 (2004) 501–509.
[8] B.S.Y. Lam, H. Yan, A novel vessel segmentation algorithm for pathological retina images based on the divergence of vector fields, IEEE Trans. Med. Imaging 27 (2008) 237–246.
[9] L. Gang, O. Chutatape, S.M. Krishnan, Detection and measurement of retinal vessels, in fundus images using amplitude modified second-order Gaussian filter, IEEE Trans. Biomed. Eng. 49 (2) (2002) 168–172.
[10] K.W. Sum, P.Y.S. Cheung, Vessel extraction under non-uniform illumination: a level set approach, IEEE Trans. Biomed. Eng. 55 (1) (Jan. 2008) 358–360.
[11] A. Osareh, B. Shadgar, Automatic blood vessel segmentation in color images of retina, Iran. J. Sci. Technol. Trans. B-Eng. 33 (Apr. 2009) 191–206.
[12] D. Marin, et al., A new supervised method for blood vessel segmentation in retinal images by using gray-level and moment invariants-basedfeatures, IEEE Trans. Med. Imaging 30 (1) (2011) 146–158.
[13] M.M. Fraz, An ensemble classification-based approach applied to retinal blood vessel segmentation, IEEE Trans. Biomed. Eng. 59 (2012) 2538–2548.
[14] E.K. Cheng, et al., Discriminative vessel segmentation in retinal images by fusing context-aware hybrid features, Mach. Vis. Appl. 25 (Oct. 2014) 1779–1792.
[15] Q. Li, B. Feng, L.P. Xie, P. Liang, H. Zhang, T. Wang, A cross-modality learning approach for vessel segmentation in retinal images, IEEE Trans. Med. Imaging 35 (2016) 109–118.
[16] P. Liskowski, K. Krawiec, Segmenting retinal blood vessels with deep neural networks, IEEE Trans. Med. Imaging 35 (2016) 2369–2380.
[17] A. Dasgupta, S. Singh, A fully convolutional neural network based structure-dprediction approach towards the retinal vessel segmentation, IEEE 14th ISBI, IEEE, Melbourne, 2017, pp. 248–251.
[18] Y. Wu, Y. Xia, Y. Song, Multiscale network followed network model for retinal vessel segmentation, in: A.F. Frangi, et al. (Ed.), MICCAI 2018, vol. 11071, LNCS, 2018, pp. 119–126.
[19] A.W. Setiawan, T.R. Mengko, O.S. Santoso, A.B. Suksmono, Color retinal image enhancement using CLAHE, ICISS, IEEE, Jakarta, 2013, pp. 1–3.
[20] A. Frédéric, K. Jean-Claude, Segmentation of vessel-like patterns using mathematical morphology and curvature evaluation, IEEE Trans. Med. Imaging 10 (2001) 1010–1019.
[21] Batch Normalization, Accelerating Deep Network Training by Reducing Internal Covariate Shift, 1502.03167.
[22] Y. Bengio, Learning deep architectures for AI, Foundat. TrendsMach. Learn. 2 (1) (2009) 1–127.
[23] J. Schmidhuber, Deep learning in neural networks: an overview, Neural Network. 61 (2015) 85–117.
[24] Boris T. Polyak, Anatoli B. Juditsky, Acceleration of stochastic approximation by averaging, SIAM J. Contr. Optim. 30 (4) (1992) 838–855.
[25] J.V.B. Soares, J.J.G. Leandro, R.M. Cesar, H.F. Jelinek, M.J. Cree, Retinal vessel segmentation using the 2-D Gabor wavelet and supervised classification, IEEE Trans. Med. Imaging 25 (2006) 1214–1222.
[26] J. Orlando, E. Prokofyeva, M. Blaschko, A discriminatively trained fully connected conditional random field model for blood vessel segmentation in fundusimages, IEEE Trans. Biomed. Eng. 64 (2017) 16–27.
[27] O. Ronneberger, P. Fischer, T. Brox, U-Net: convolutional networks for biomedical image segmentation, in: N. Navab, J. Hornegger, W.M. Wells, A.F. Frangi (Eds.), MICCAI 2015. LNCS, vol. 9351, Springer, Cham, 2015, pp. 234–241 https://doi.org/10.1007/978-3-319-24574-4 28.
[28] F. Zana, J.C. Klein, Segmentation of vessel-like patterns using mathematical morphology and curvature evaluation, IEEE Trans. Image Process. 10 (7) (Jul. 2001) 1010–1019.
[29] X.Y. Jiang, D. Mojon, Adaptive local thresholding by verificationbased multi threshold probing with application to vessel detection in retinal images, IEEE Trans. Pattern Anal. Mach. Intell. 25 (1) (Jan. 2003) 131–137.
[30] A.M. Mendonca, A. Campilho, Segmentation of retinal blood vessels by combining the detection of centerlines and morphological reconstruction, IEEE Trans. Med. Imaging 25 (9) (Sep. 2006) 1200–1213.
[31] M.S. Miri, A. Mahloojifar, Retinal image analysis using curvelet transform and multistructure elements morphology by reconstruction, IEEE Trans. Biomed. Eng.

58 (5) (May 2011) 1183–1192.

[32] B.S.Y. Lam, Y.S. Gao, A.W.C. Liew, General retinal vessel segmentation using regularization-based multiconcavity modeling, IEEE Trans. Med. Imaging 29 (7) (Jul. 2010) 1369–1381.

[34] T. Mapayi, S. Viriri, J.R. Tapamo, Adaptive thresholding technique for retinal vessel segmentation based on GLCM-energy information, Comput. Math. Methods Med. 2015 (2015) 597475.

[35] M. Niemeijer, J. Staal, B. van Ginneken, M. Loog, M. D. Abramoff,"Comparative study of retinal vessel segmentation methods on a new publicly available database, Image Process, Med. Imaging 5370 (2004) 648–656 2004.

[36] A. Hoover, V. Kouznetsova, M. Goldbaum, Locating blood vessels in retinal images by piecewise threshold probing of a matched filter response, IEEE Trans. Med. Imaging 19 (3) (Mar. 2000) 203–210.

[37] J. Odstrcilik, et al., Retinal vessel segmentation by improved matched filtering: evaluation on a new high-resolution fundus image database, IET Image Process. 7 (4) (2013) 373–383.

[39] Andrew L. Maas, Awni Y. Hannun, Andrew Y. Ng, Rectifier nonlinearities improve neural network acoustic models, Proceedings of the 30th International Conference on Ma-Chine Learning, Atlanta, Georgia, USA, vol. 28, JMLR: W&CP, 2013.